This is a repository copy of *Novel application of ground penetrating radar for damage detection in thick FRP composites*.

White Rose Research Online URL for this paper:
https://eprints.whiterose.ac.uk/221322/

Version: Published Version

Novel application of ground penetrating radar for damage detection in thick FRP composites

James A. Quinn *, Ourania Patsia, Antonios Giannopoulos, Conchúr M. Ó Brádaigh, Edward D. McCarthy

School of Engineering, Institute for Materials and Processes & Institute for Infrastructure and Environment, The University of Edinburgh, Edinburgh, EH9 3FB, UK

ARTICLE INFO

ABSTRACT

This paper presents the first successful application of ground penetrating radar (GPR) to the inspection of thick (≥100 mm) fiber-reinforced composites. These thick composites are found in wind/tidal turbine blades and composite-hulled ships, where sufficient non-destructive testing (NDT) remains challenging. Polyester-glass specimens, ranging in thickness from 100 to 120 mm, were created with delamination-mimicking damage. Specimen thickness, damage depth location, antenna orientation and damage dryness were the test variables. Finite-difference time-domain simulations indicated the method's feasibility, and experimental results confirmed these findings. GPR effectively detected and precisely located dry, in-plane damage, with increased detectability for water-filled damage due to the enhanced contrast of electrical properties that creates the damage response in the signal. This capability is particularly advantageous for marine composites, where extensive damage may lead to water ingress. In a comparison with an ultrasonic inspection, GPR proved superior for the thicker composites (≥100 mm). As the first successful application of GPR to composite structures, these findings significantly advance the field of NDT of these materials.

1. Introduction

Non-destructive testing (NDT) techniques are utilized to evaluate the condition of components without compromising their structural integrity. For asset maintenance, NDT techniques have been integrated into established operational programs to probe the structural integrity of components throughout their service life. Although NDT of fiber-reinforced polymer (FRP) components for damage detection (e.g., detection of delaminations, cracks and debonds) has been extensively covered in the literature [1–3], the existing body of work mainly focuses on thin (≤15 mm) laminate structures that are commonly used in the aerospace industry. Conversely, many wind/tidal turbine blades, military vehicles, ships and other seafaring vessels contain thick (≥20 mm) FRP laminates [4–6]. Furthermore, few NDT techniques have been proven to work on ultra-thick (≥100 mm) FRP laminates, and adequate NDT of these structures remains a significant challenge. In particular, some difficulties associated with detecting damage features in ultra-thick FRPs are: (a) that damage is typically small in size compared to the size of an ultra-thick FRP structure, and (b) the inspection is made more complicated by the different FRP constituent materials having different properties (e.g., acoustic, thermal, mechanical). Ultrasonic testing (UT) methods (including "advanced" ultrasonic methods,

e.g., array-based techniques, sophisticated collection and processing regimes etc.) are commonly used in industry. Since many polymeric materials are highly-damping, an intrinsic challenge in the UT of thick FRPs is that low inspection frequencies (≤1 MHz) are required to achieve penetration. However, low frequency UT methods typically have poor spatial resolution capabilities [7–9]. This can result in complications when targeting relatively small features in thick FRPs. Whilst UT methods are common for the inspection of thick FRPs, increasing the laminate thickness makes successful ultrasonic inspection much more challenging [10–13]. Since the UT of FRPs is a mature field, with time, improving the efficacy of this technique is likely to become increasingly non-trivial.

Ground penetrating radar (GPR) is a mature NDT technique [14] that has many applications, including: concrete scanning [15]; bridge and road inspection [16]; geological applications [17]; landmine detection [18] and planetary studies [19]. GPR detects contrasts in dielectric properties between materials, and has been extensively used for mapping buried targets — including structural damage — provided there is sufficient contrast between their properties and the surrounding material.

GPR employs a transmitting antenna to send ultra wideband electromagnetic (EM) pulses into materials. In contrast to conventional

---

radars, the propagation of GPR EM waves through the inspected materials is complicated by the material properties, which affect the EM wave velocity and attenuation. Both of these factors are dictated by the dielectric properties of the inspected materials. The dielectric properties are: the electric permittivity ε (which has the largest influence on the EM wave velocity in a given medium), the electric conductivity σ (which relates to the attenuation) and the magnetic permeability μ. The permittivity of a material is usually described with respect to the permittivity of free-space, and is often stated as a relative permittivity ε_r. When there is a contrast in the dielectric properties between materials, part of the EM energy is reflected and recorded by a receiving antenna [14,20]. After acquiring and processing the received signal, information about the structure and the nature of materials or other targets can be obtained.

The center frequency of the GPR transducer determines the trade-off between penetration depth and resolution, and is chosen based on the type of survey and targets being sought. A high center frequency antenna transmits shorter pulses that allow for higher resolution and are able to resolve smaller targets, but at the expense of a relatively small penetration depth. In contrast, lower center frequency GPR antennas transmit broader pulses that have the ability to penetrate at greater depths, but at the cost of lower resolution. Therefore, for near-surface surveys where the objective is to detect relatively small targets — such as damage inside an FRP — a high frequency antenna should be used.

In the literature, common research themes consist of various radar systems in the 1–3 GHz range that are used to inspect FRP reinforced concrete and externally bonded FRP-concrete structures [21–24]. In such cases, the inspection targets were either interfacial debonds in the FRP-concrete bondline, or defects present inside the concrete. One notable use of GPR by Hing and Halabe [25], was to inspect the bondline between an externally bonded polymer-concrete wear surface and a glass FRP bridge deck (totaling 101.6 mm thick). A 1.5 GHz ground coupled antenna was used to search for calibrated defects in the bondlines in the structure. Research with similar characteristics — with respect to GPR equipment and inspected structure — have been reported elsewhere, e.g., [26], each describing similar results. In Hing and Halabe [25], the bridge deck construction was of a hollow rectangular cell design where the 11.43 mm upper and lower decks (the flanges) were separated by a 139 mm air gap using 10.16 mm thick webs. The 9.5 mm thick polymer-concrete wear surfaces were bonded to the deck flanges, and debonds (both dry and water filled) were simulated in the bondline. Photographs of the inspected structure can be found in Ref. [26]. Infra-red thermography was included as a correlative technique, so that the effectiveness of GPR in detecting close subsurface delaminations could be assessed. Water-filled delaminations were detected at the top deck, however, the researchers were unable to precisely locate the water-filled debond at the lower deck; this was attributed to increased radar echo at depth. Additionally, regardless of their location, the dry debonds could not be detected using GPR. The detection of the water-filled debonds in the structure is consistent with the high relative permittivity of water (approximately 80 at 20 °C [27]) in relation to concrete (approximately in the range from 4 to 10 [20]) and most polymers (approximately in the range from 2 to 10 [28]), and therefore, becomes a predictable result. When considering the relative permittivity of air (1 [27]) in comparison to the bridge FRP materials, it is logical that the air cracks or disbonds would be challenging to detect, due to insufficient contrast in the dielectric properties and/or due to the 1.5 GHz GPR system that was used not being able to resolve such small debonds. Although this literature is concerned with debonds between concrete and FRPs — rather than damage within the FRP — the findings within are still somewhat indicative of the applicability of the particular GPR equipment to thick FRP structures.

Due to the limitations of each NDT technique, a common theme in NDT research is that no single technique enables the complete inspection of FRPs [29]. Several sources agree that the complete inspection of FRPs often necessitates the combination of more than one

NDT technique. Since the literature demonstrates that GPR is used in other applications to penetrate much deeper than existing FRP inspection techniques (e.g., UT) and that GPR should not be affected by polymer-fiber interfaces within the FRP, it could be well positioned to complement existing inspection methods. Several authors have speculated about the possible application of GPR to FRP inspection in literature reviews [11,29,30]. However, no corresponding published research or experimental data has been found. As such, there is presently a knowledge gap on whether GPR can be used to inspect FRPs. Therefore, the FRP user community could be unnecessarily missing out on an effective, complementary solution to a long-standing issue: detection of damage in thick and ultra-thick FRPs.

In this paper, GPR is applied to ultra-thick glass FRP specimens to test its efficacy in detecting damage in FRP structures. Due to the nature of the problem, which requires a high frequency GPR transducer, the GPR data was collected using the 2000 MHz "palm" antenna from Geophysical Survey Systems, Inc (GSSI) [31]. Numerical modeling of the EM fields propagating in the glass FRP material was utilized to provide insight and enhance the interpretation of the real responses. Thereafter, the numerical modeling was verified in a series of experimental inspections of real FRP specimens using a real GPR antenna. Finally, the GPR experimental inspection data was compared with UT inspection data of the same FRP specimens that was previously reported in the literature. Given the present lack of publications where GPR has been used to inspect for damage in glass FRP structures, the findings presented in this paper constitute original research on the applicability to — and efficacy of — GPR in this context.

2. Methodology

2.1. Approach for evaluating GPR efficacy

Multiple approaches were used to determine the efficacy of GPR in detecting FRP delamination damage. Firstly, a 3D numerically equivalent model of the experimental GPR inspection was implemented to assess the feasibility of the technique (for further details, see Section 3). Thereafter, an experimental approach was implemented where a real GPR system was used to collect experimental inspection data from thick glass FRP specimens (for further details, see Section 4). In the final part of this showcase, the data collected from the GPR experimental inspections were compared to data collected using a modern ultrasonic testing system. Variables used in the comparison of GPR and ultrasound were the number of damage features detected by each technique, as well as the accuracy of each technique in measuring the depth of detected damage within each FRP specimen. Note that the focus herein is detecting delamination damage and not manufacturing-induced flaws, e.g., voids. Since manufacturing-induced flaws are typically much smaller features, it is likely that their detection would be difficult using any GPR setup.

2.2. Description of the GPR system

A GSSI 2000 MHz "palm" antenna (Fig. 1(a)) was selected, which has a typical depth range of 0 to 300 mm, depending on the material and environmental conditions, and antenna dimensions of 91.5 × 91.5 × 105 mm [31]. In order to ensure the best possible resolution (i.e., to resolve delaminations at the expense of penetration depth), the study used the highest frequency antenna available from the present resources. Given the comparatively small penetration depth required for this use case (120 mm), relative to the antenna — maximum — specification, this compromise was considered favorable. Both the transmitting (Tx) and the receiving (Rx) antenna are in the same enclosure at a fixed distance from each other — as indicated in Fig. 1(b) — meaning that the data collection mode is the Common Offset (CO) method.
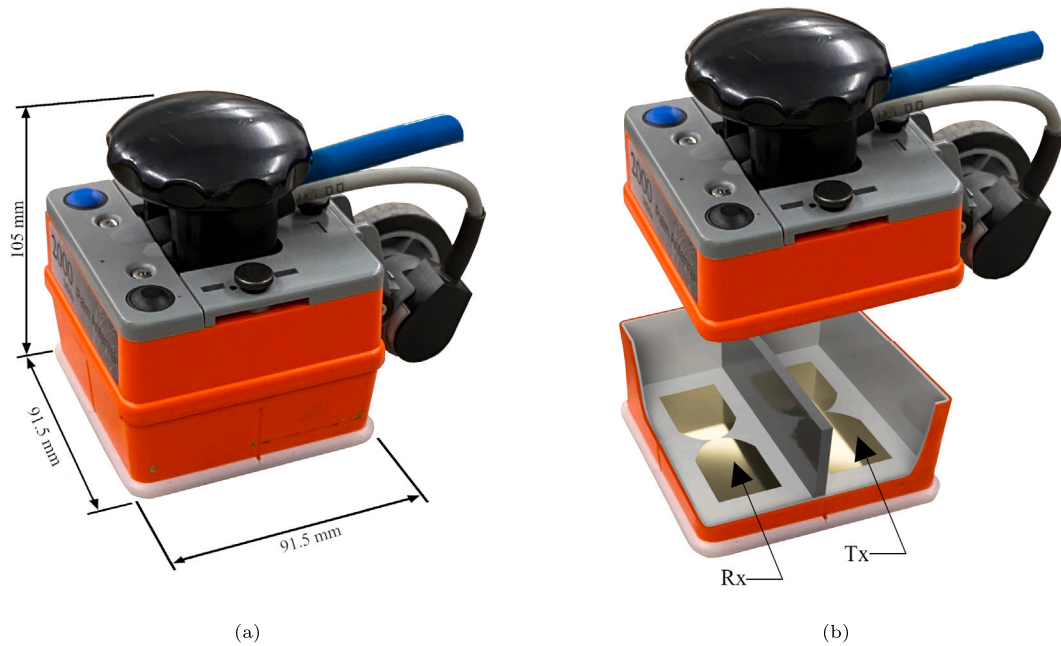
Fig. 1. Schematic of the GSSI 2000 MHz palm antenna: (a) Regular view in as-used configuration (dimensions in mm). (b) Illustrative exploded view indicating the relative position and size of Tx and Rx antennae within the unit.

2.3. FRP specimen designs used for the showcase

For the purposes of this showcase, two thick FRP laminate specimens were used as shown in Fig. 2. These specimens were originally used in studies by the same authors concerning damage detectability in FRPs using an ultrasonic method [10,32]. In line with typical marine composite structures (e.g., minehunter ships) isophthalic polyester resin and 800 g m^{-2} plain weave glass reinforcement mat were chosen as the FRP constituent materials. The two specimens were regular cuboidal in shape, and had thicknesses of 100 mm and 120 mm, respectively. Three delamination-mimicking features (henceforth referred to as "damage") were included in each specimen, and the dimensional details of these are also included in Fig. 2. The damage features were 3 mm thick, and were included at various depths throughout each specimen.

Whilst 3 mm thick delaminations could be described as large relative to damage typically found in real applications, this dimension was selected to represent a more severe case of accumulated service damage. Since no research exists on using GPR to detect damage in FRPs, this approach facilitated the evaluation of GPR as a damage detection technique for FRPs with a high degree of confidence. Furthermore, features with similar through-thickness dimensions have been reported in FRP NDT research, e.g., in Ref. [33]. The delamination damage used in the present study was designed in a step-like shape pattern because these specimens were originally designed for a study on concerning ultrasound inspection of thick FRPs in Refs. [10,32], however, the step-like shape was not utilized in the present study. With these specimens, it was possible to evaluate the general ability of GPR to detect a range of delamination damage locations in a typical marine FRP.

The material system and manufacturing techniques employed in this study were chosen to mirror those commonly used in marine industries. As previously mentioned, a mixture of Crystic 489PA isophthalic polyester resin and Butanox M50 methyl ethyl ketone peroxide crosslinking initiator (at a volume fraction of 2%) was blended and subsequently used to saturate the reinforcing fibers. The reinforcement consisted of a plain woven glass mat with a weight of 800 g m^{-2}; additional chopped strand glass mat with a weight of 300 g m^{-2} was added as needed to compensate for crimp accumulation and ensure consistent
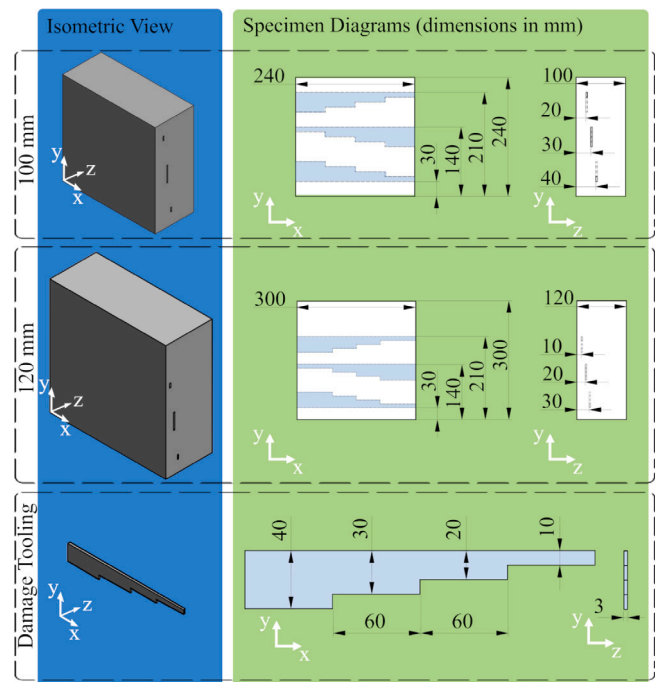
Fig. 2. FRP specimen diagrams with damage locations and damage tooling pattern dimensions.

specimen thickness. The curing cycle was 24 h at room temperature (20 °C) with no additional environmental control or post-curing steps.

Two glass FRP specimens were produced by layering fiber mats in a warp-on-warp arrangement, followed by impregnation of the resin mixture using brushes, plastic wedges, and rollers. Detailed FRP specimen geometry diagrams, indicating the locations and depths of all damage, can be found in Fig. 2. The fiber volume fraction (V_r) was controlled in each ply by evenly distributing the liquid resin until a fiber volume fraction of approximately 45% was reached—calculated using the equation $V_r = (M_r) \times 100 \times (\rho_c/\rho_r)$ (transcribed from ASTM
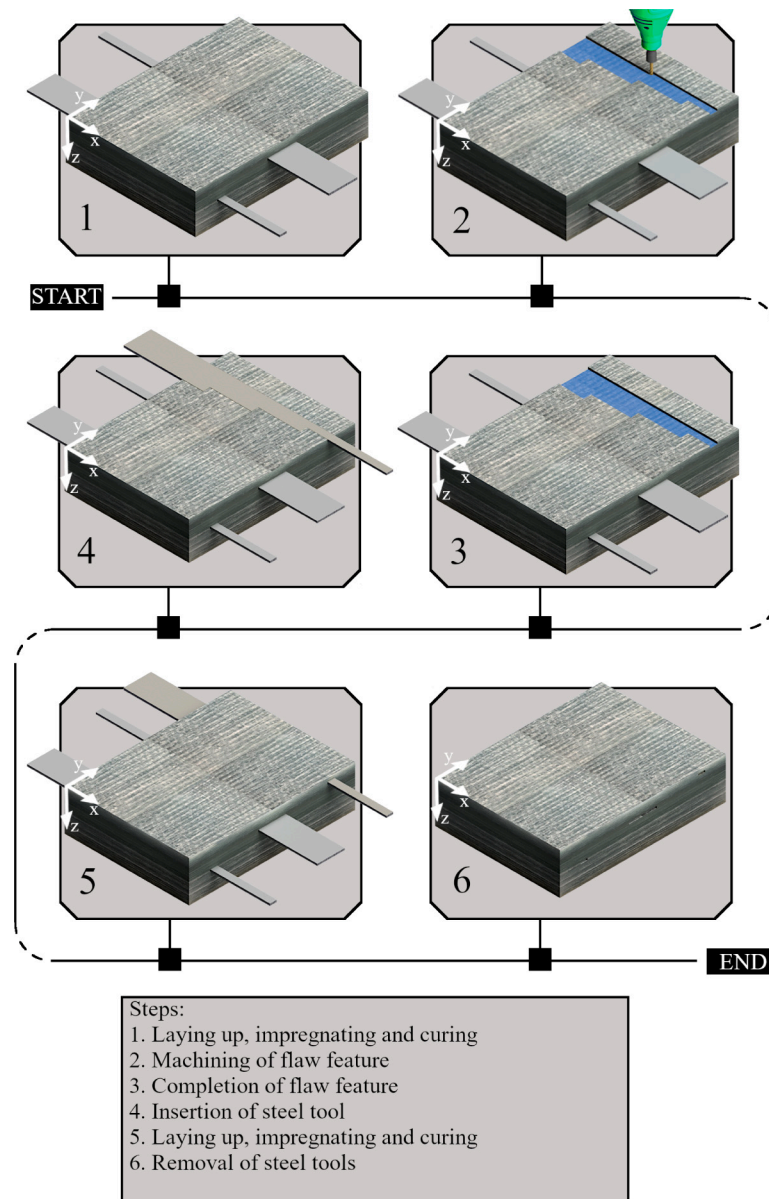
Fig. 3. Schematic of the specimen manufacturing process.

D3171-15) where M_r is the mass ratio of reinforcement in the ply, ρ_c is the density of the cured composite (1.9 g cm^{-3}), and ρ_r is the density of the reinforcement. A schematic representation of the process for creating artificial damage in specimens is illustrated in Fig. 3. To create artificial damage in the specimens, the lay-up process was temporarily paused at specific part thicknesses. Once the resin had fully cured, rotary tools and manual files were utilized to create a 3 mm deep recess on the current top surface of the part. Steel male tooling counterparts, machined in a similar pattern and coated with Loctite Frekote NC770 mold release agent, were then inserted into the recesses. The lay-up process was then resumed until the next target depth was achieved, or until the specimen was completed. After the final curing, the steel tools were removed from the specimens, resulting in consistently shaped cavities. To facilitate easy removal of the steel tools, a slight draft angle was added to all sharp edges of the tools, allowing them to be gently tapped out with a nylon-headed hammer.

2.4. Approach for GPR scanning (modeling and experimental)

Data were collected in the time domain over a time window of 6 ns, with 512 samples per A-scan. No filtering was applied during collection i.e., only raw data were stored. Compared with other NDT techniques, an additional consideration in GPR is that GPR antennas radiate EM energy with a preferred polarity. In the GSSI 2000 MHz "palm" antenna, the Tx and Rx antennas are placed parallel to each other in the enclosure, and both are therefore perpendicular to the scanning direction. This antenna arrangement is the most commonly used and is called perpendicular broadside [34]. In the present work, when the scanning direction is along the specimen y axis (Fig. 4), the Tx and Rx are oriented so that the electric field is polarized parallel to the x axis. When the scanning direction is along the specimen x axis (Fig. 4), the Tx and Rx are oriented so that the electric field is polarized parallel to the y axis. For this reason, two scanning directions were considered in the present work: (I) scanning perpendicular to the direction of the damage (denoted by ⊥), and (II) scanning parallel to the
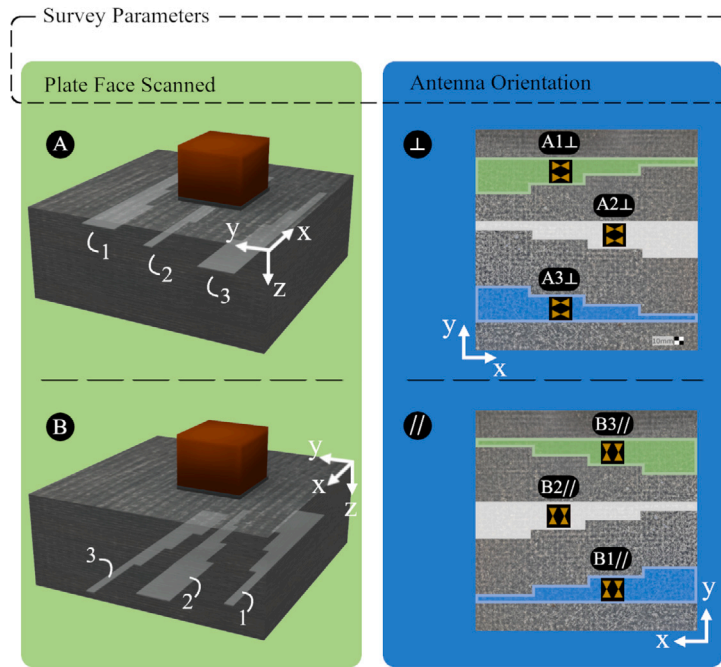
Fig. 4. Schematic showing survey parameters and damage/scanning naming convention.

direction of the damage (denoted by //). In both the model and the real experiments, specimens were scanned firstly on the front face, denoted A side (with the damage closest to the antenna), and once data had been captured, the specimens were turned over to be scanned from the opposite face, denoted B side, where the damage features were furthest from the antenna. The scanning process and damage/scanning naming convention are shown in Fig. 4.

2.5. Approach for processing GPR data (modeling and experimental)

In GPR, responses from features (e.g., frontwall, backwall, damage) are normally indicated in B-scans by the presence of three-stripe patterns (e.g., white-black-white or black-white-black bands). These patterns result from the radiation characteristics of a dipole antenna, where each response consists of three half cycles of positive-negative-positive or negative-positive-negative amplitudes [35]. The first case of positive-negative-positive pattern is considered to have a positive polarity, whereas the latter a negative polarity. The polarity of the received signal is determined by the change in the dielectric properties from one medium to another; going from a higher permittivity medium to a lower or vice versa. As an example, Fig. 5(a) illustrates a raw experimental B-scan collected from the damage 120A1 (from the 120 mm specimen). The first response (i.e., the first white-black-white band) shown in the image is from the direct wave, which consists of the direct air wave and the direct ground wave merged together. The direct air wave is the wave traveling directly from the Tx to the Rx, while the direct ground wave is the wave that travels along the air-FRP frontwall interface from Tx to Rx. In GPR signals, these responses usually arrive very close in time and cannot be separated. This response, along with the response from the backwall-air interface can be clearly seen in Fig. 5(a). Unfortunately, the response from the 120A1 damage cannot be easily seen in Fig. 5(a). This is because the direct wave signal is strong enough to mask the response from the damage, which has a weaker signal.

For this reason, a background removal filter [36] was applied to remove the direct wave response. For this purpose, average background removal [37] was utilized, whereby a range of A-scans from the appropriate reference specimen were averaged and subsequently subtracted from each test A-scan, with a necessary time-gating of the reference

signal to retain the backwall response. Eq. (1) was used for the average background removal, where A is the A-scan, x is the xth A-scan, T is the number of samples, M is the number of collected A-scans and A_{ref} represents a reference A-scan. This mean signal represents the background response, which when subtracted, allows for the response from the damage to become more evident.

$$A(x, 1 : T) = A(x, 1 : T) - \frac{1}{M}\sum_{i=1}^{M} A_{ref}(i, 1 : T) \qquad (1)$$

After background removal, the returned responses of the damage, although visible, are still weak in amplitude. Gain is required to amplify the damage responses and make them more easily detectable. An example of the output from background removal and gain adjustment is given in Fig. 5(b) for the 120A1 damage. Comparing Figs. 5(a) to 5(b), the data processing has removed the direct wave response from the B-scan, facilitating easy identification of the 120A1 damage response in the B-scan in Fig. 5(b). Due to the success of this data processing regime, the same processes of background removal followed by gain adjustment were applied to all response data throughout this work, in both the modeling and the real experimental parts.

3. Numerical modeling

Numerical modeling of GPR in 3D was initially utilized to assess the performance of GPR in inspecting FRP materials, and thereafter, to inform the real experimental inspections. Modeling was performed using gprMax, an open source finite-difference time-domain (FDTD) solver [38]. In order for the simulations to be as representative as possible to the real responses, a 3D model of the GSSI 2000 MHz "palm" antenna (as developed in the literature [39,40]) was included in the simulations.

In the models, "inspections" of both specimens were simulated to determine whether the damage could be detected. Since this approach has been extensively validated in the literature for other use cases, these models helped to evaluate the feasibility of the technique, and thereafter, to inform the subsequent real, experimental approach. In the model, the domain size was set to $350 \times 350 \times 267$ mm, which included the antenna model, the FRP specimen and the surrounding air, with a fine step size of 1 mm, in accordance with the antenna model
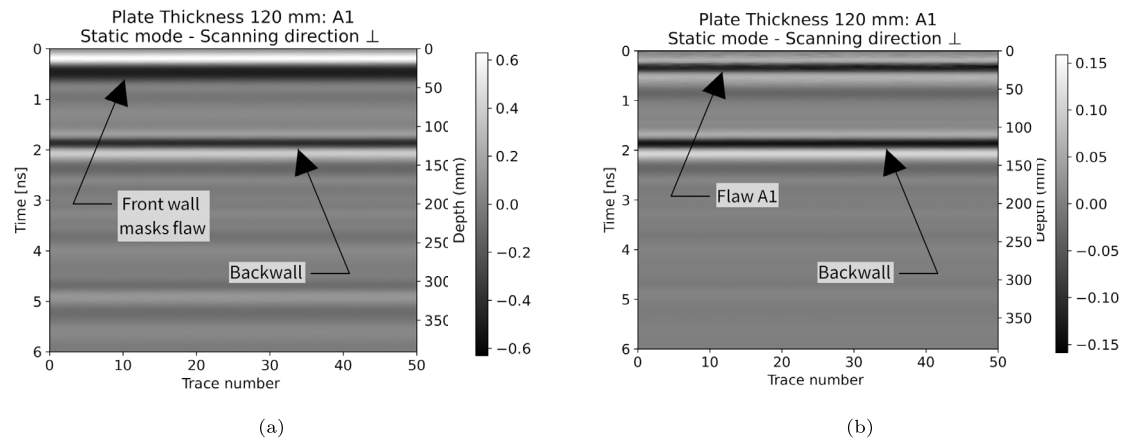
Fig. 5. Representative B-Scans from experimental data, demonstrating the efficacy of background removal: (a) Damage 120A1⊥ raw data. (b) Damage 120A1⊥ post-processed data.

mesh optimization that was performed in Ref. [41]. Inspections were modeled with the digital equivalent antenna positioned directly above each damage in turn (e.g., as shown in Fig. 4). To maximize the number of inspection scenarios, inspection was considered from both sides of each specimen, termed the A side and the B side. An example of the modeling process taken from the model of the 120 mm specimen, is shown in Figs. 6(a), 6(c) and 6(d) for the 120 mm reference case, the 120 mm A side and the 120 mm B side, respectively. Synthetic data were generated over a time window of 6 ns, i.e., identical to the time window used when collecting the experimental GPR responses. The simulated FRP specimens had the same dimensions as the subsequent real specimens, and were modeled as finite homogeneous isotropic material, since there exists negligible contrast of the electrical properties of the different FRP constituents. In addition, for the same FRP material system, varying the lay-up sequence of an inspected specimen would have negligible effect on the responses, since the dielectric properties of the constituents would remain unchanged. For other FRP material systems not included in the present work, the electrical properties of the different FRP constituents may have sufficient contrast, so that modeling the system as inhomogeneous is required. If necessary in future works, any required geometrical complexities could be introduced into the model in gprMax. All materials within the present work were non-magnetic and were modeled with relative permeability $\mu_r = 1$. Each damage was modeled with $\varepsilon_r = 1$ and $\sigma = 0$ S m^{-1}, which are the dielectric properties of air. The FRP specimens were modeled with a relative permittivity of $\varepsilon_r = 4.5$ (as calibrated from the real reference specimen) and with a conductivity of $\sigma = 0$ S m^{-1}, since measured values for polyester FRP conductivity found in the literature are in the order of 4×10^{-5} to 5.5×10^{-5} S m^{-1} at 400 kHz [42]. This was considered reasonable since glass-FRPs are widely accepted as electrically insulating materials [43–46]. Preliminary trials showed no significant difference when these published values were used in the model, when compared to setting $\sigma = 0$ S m^{-1}, therefore, $\sigma = 0$ S m^{-1} was selected as an appropriate simplification. Note that even with $\sigma = 0$ S m^{-1}, there are still other loss mechanisms that contribute to the total signal loss and reduction in the received amplitudes, e.g., geometrical spreading and scattering. Lastly, each modeled B-scan took approximately 300 s on 4 NVIDIA TITAN RTX 24 GB GPUs.

To be directly comparable, identical data processing steps were applied to both modeled responses and the experimental data (for more details, see Section 2.5). As an example of the modeling, the modeled responses from the 120 mm reference specimen, the 120A2 and the 120B2 damage, are shown in Figs. 6(b), 6(d), and 6(f), respectively. The response from the backwall of the specimen is present in all data, as annotated in the figures. After processing, the responses from the damage are clearly detectable in both Figs. 6(d) and 6(f), as annotated. The reflection from 120A2 is more easily distinguished due to its

greater amplitude and arrival earlier in time, whereas the reflection from 120B2 is less clear due to propagation losses and being very close to the backwall. Due to their similar arrival time, the response from 120B2 cannot be distinguished from the response from the backwall, however, there are clear amplitude differences when comparing with the reference case. These amplitude differences are indicative of an additional target existing in the vicinity of the backwall, which can be attributed to the 120B2 damage. The above provide an indication that small damage existing in glass-FRPs can be detected with a high-frequency GPR system, and more specifically, that the GSSI 2000 MHz "palm" antenna can be used to detect such damage, since a realistic model of the GPR transducer was used in the simulations.

4. Experimental verification

4.1. Collection of GPR experimental data

Initially, the antenna was held stationary on each specimen in turn, at a location within the specimen which had been verified as damage-free. This enabled the collection of a reference scan of a damage-free area for each specimen, against which all later scans could be compared. Furthermore, the reference scans provided a fundamental route towards a depth-measurement calibration process; the EM wave velocity through the FRP was calculated using the measured two-way travel time of the waves between the antenna and the backwall in the (known thickness) reference cases. The reference scans from both specimens resulted in similar EM wave velocity values ($v = 0.141 \pm 0.001$ m ns^{-1}), from which the relative permittivity of the composite material was estimated ($\varepsilon_r = 4.5$), using the equation $v = c/\sqrt{\varepsilon_r}$ given in [47], where c is the speed of light. This estimate of the velocity would later be used to obtain the depths of each damage inside the specimens. After collecting the reference scans, the antenna was held stationary over an identified damage, while raw data was captured and recorded on the controller for later processing. In all cases, the GPR transducer was placed directly on the FRP specimen to maximize energy going into the material, as shown in Fig. 7. For each damage location on the specimen, multiple A-scans were collected in time mode and merged to produce a B-scan.

4.2. Results and discussion

4.2.1. Detecting FRP damage using GPR (experimental)

Example experimental A-scans for damage 100A2⊥ and 120A2⊥ are shown in Figs. 8(a) and 8(b), respectively. The presence of the damages is clearly identifiable, as they cause increases in the signal amplitudes in the early part of the A-scans. The deviation of the A2⊥ waveforms, away from the relevant reference direct wave response, is caused by the
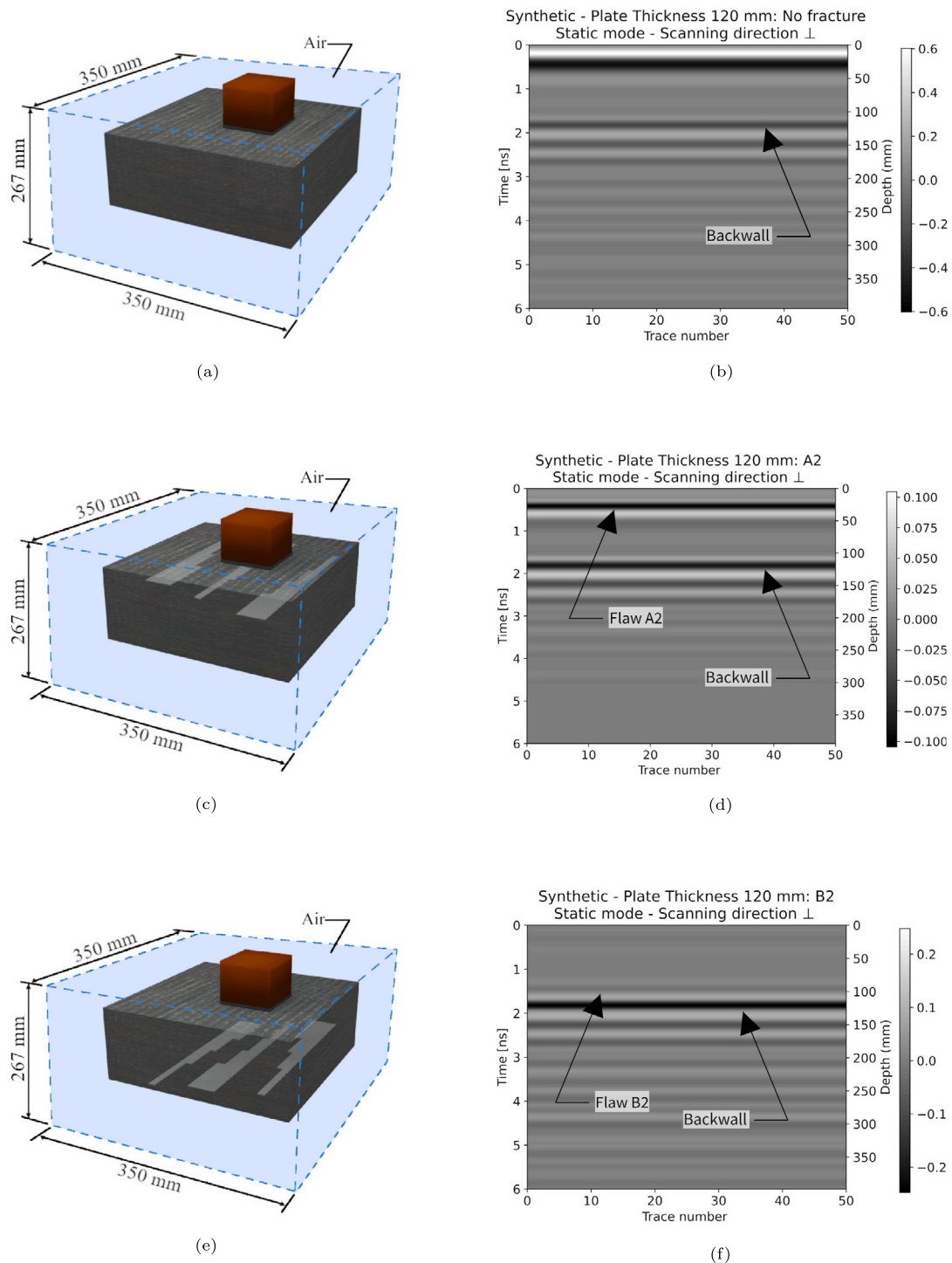
Fig. 6. Examples of the outcomes from the modeling using gprMax: (a) Schematic of the environment for the synthetic no damage reference case. (b) Synthetic B-Scan for the no-damage reference case. (c) Schematic of the environment for the synthetic 120A2⊥ damage. (d) Synthetic B-Scan for the synthetic 120A2⊥ damage. (e) Schematic of the environment for the synthetic 120A2// damage. (f) Synthetic B-Scan for the synthetic 120A2// damage.

addition of the responses from the respective A2 damage. The responses that arrive later than the backwall in time, are due to the responses from the specimen edges (where a gradient of permittivity between specimen and air has been detected, but the response traverse path from edge to detector is larger than the specimen depth, and therefore the response arrives later in time) and/or multiples. These clutter responses may not be received when scanning a larger structure, e.g., minehunter ships or turbine blades.

Although amplitude differences exist between the reference and the damage responses in the raw experimental data, with raw data alone, only 4/12 damage features were identified in each specimen, respectively. As numerical modeling had showed similar responses, the background removal and gain adjustment processes (Section 2.5) were also applied to the experimental data. After these data processing steps, the number of damage features that were detected increased to 11/12 in each specimen. Full details of the ability to detect for
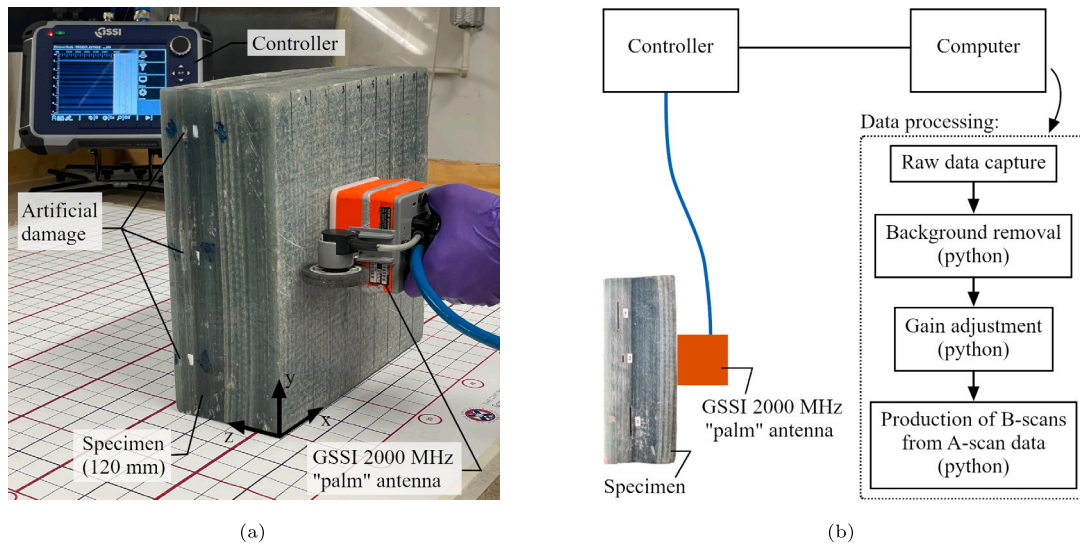
Fig. 7. Experimental configuration for GPR survey: (a) Photograph showing the experimental survey setup. (b) Schematic for the experimental configuration and flowchart for the data processing regime.
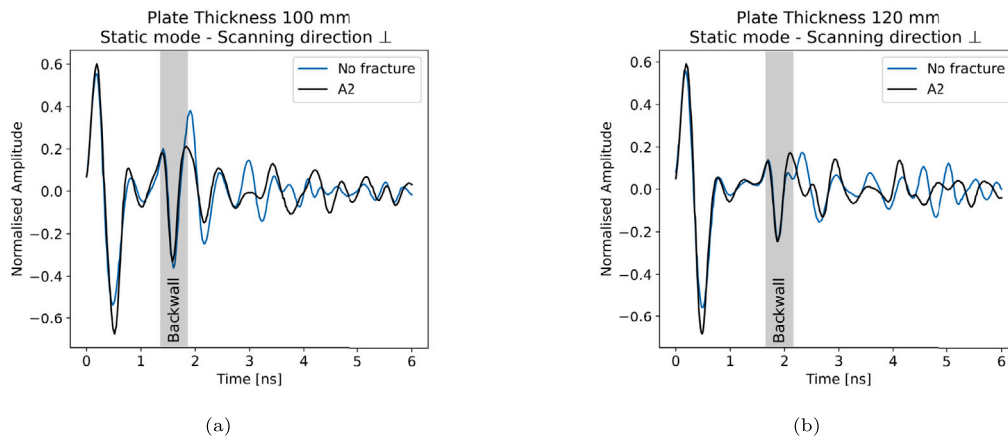
Fig. 8. Representative A-Scans from experimental data: (a) Damage 100A2⊥. (b) Damage 120A2⊥.

each damage/antenna-orientation combination are included in Table 1, demonstrating the complete success of the background removal process. The (processed) results for the specimens with dry damage features, are presented in Fig. 9 (100 mm specimen) and Fig. 10 (120 mm specimen), with the general format:

(a) The relevant reference specimen with no damage, as viewed from the probed face, with the antenna position indicated figuratively.

(b) Processed B-scan for the given reference case.

(c) The damage specimen as viewed from the A side, with the position of each damage overlaid and the various antenna positions figuratively indicated. Each antenna location/orientation was used sequentially to capture data and is indicated figuratively (not to scale).

(d) Processed B-scan for the damage A2⊥.

(e) The damage specimen as viewed from the B side, with the position of each damage overlaid and the various antenna positions figuratively indicated. Each antenna location/orientation was used sequentially to capture data and is indicated figuratively (not to scale).

(f) Processed B-scan for the damage B2⊥.

Fig. 9 demonstrates the results for the 100 mm specimen. The responses from damage 100A2 and 100B2 are both identified in Figs. 9(d)

and 9(f) after background removal, with 100A2 being easier to detect — due to larger amplitude and its arrival earlier in time — than 100B2, which is weaker, deeper and very close to the backwall. Similarly, Fig. 10 demonstrates the results for the 120 mm specimen, where the responses from damage 120A2 and 120B2 are both identified in Figs. 10(d) and 10(f) after background removal. Again, 120A2 is easier to detect — due to larger amplitude and its arrival earlier in time — than 120B2, which is weaker, deeper and very close to the backwall. These results are analogous to the output from numerical modeling, reinforcing the evidence that GPR can be used for damage detection in thick glass FRPs.

4.2.2. Depth measurement accuracy (experimental)

For further confirmation of the ability to resolve damage at various depths, an example of the complete inspection of one side of the 100 mm thick specimen is shown in Fig. 11. Fig. 11(a) shows a representative sketch of the antenna position during the inspection of each damage location, while Figs. 11(b)–11(d) show the B-scans over locations 100A1, 100A2 and 100A3, damages respectively. With respect to the B-scans shown in Figs. 11(b)–11(d), the response from each damage feature was clearly identifiable. Furthermore, the response from each damage feature arrived at a different time, corresponding to the different depthwise location of each damage.
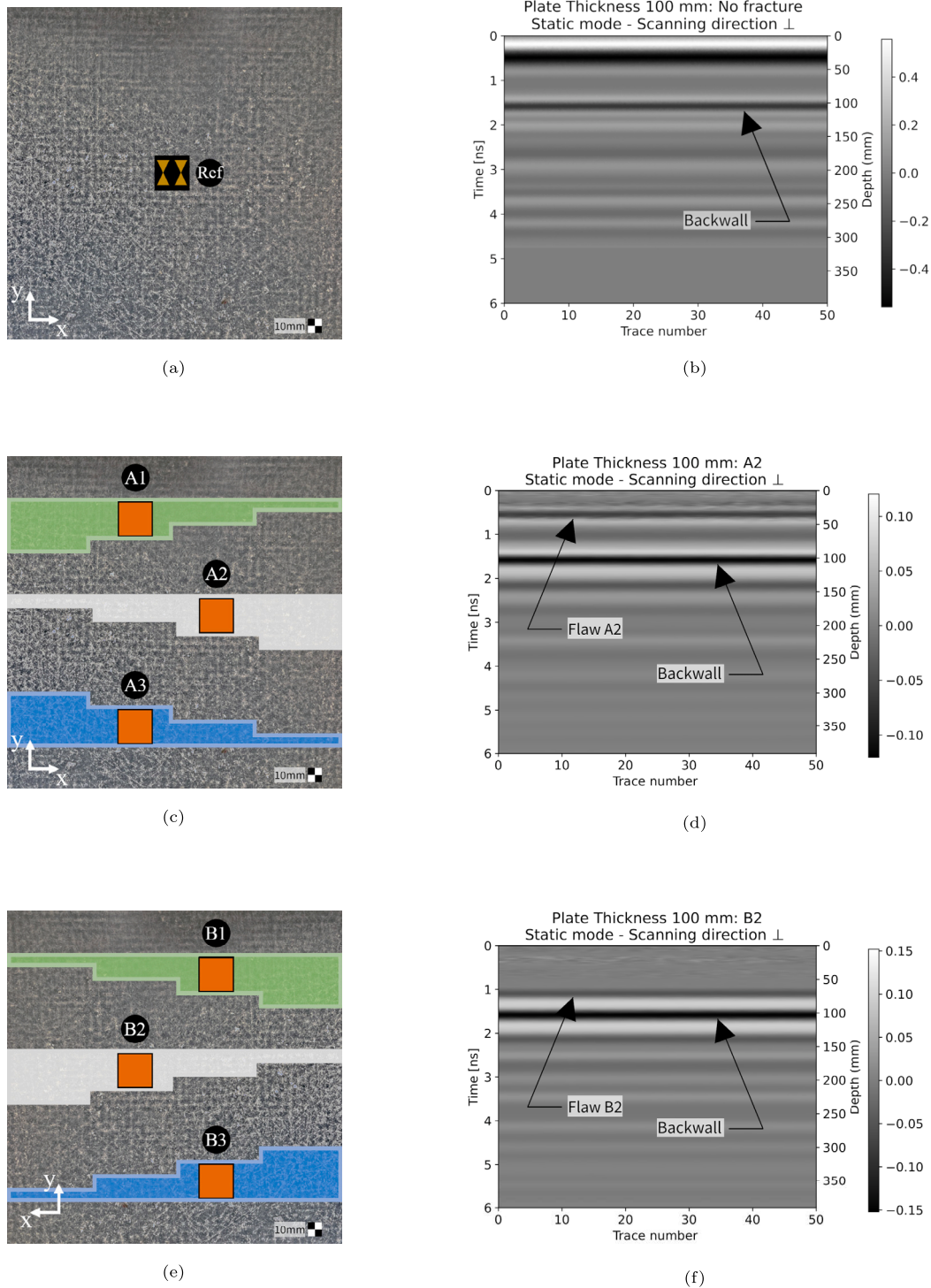
Fig. 9. An example of experimental data collection for the 100 mm specimen: (a) Location of reference scan. (b) Reference B-scan in a location having no damage. (c) Antenna static locations for the A-side. (d) B-Scan of the location 100A2⊥. (e) Antenna static locations for the B-side. (f) B-Scan of the location 100B2⊥.

Since the GPR was able to distinguish the different arrival times of the damage responses, the depthwise location of each identified damage in the test matrix was calculated using the speed-distance-time relationship, as described in Section 4.1. The GPR-measured damage depths are compared to real damage depths in Fig. 12, to evaluate the accuracy of the technique. The 1:1 dashed line in Fig. 12 traces the line at which GPR-measured damage depths would be exactly equal to real damage depths, in other words, at 100% measurement accuracy. As can be seen, for the detected damages, the depth measurements from

both the perpendicular and parallel antenna orientations are in good agreement with the absolute, real damage depths. As with other NDT techniques (e.g., UT), worse accuracy of depth measurements would be expected for deeper damage features, because the propagation losses and the frequency constraints of the system result in loss of resolution. However, Fig. 12 shows that these factors did not have significant effects on the accuracy of damage depth measurement. At the feature depths, and for the antenna system used in the present study, the propagation losses and the frequency constraints of the system were not
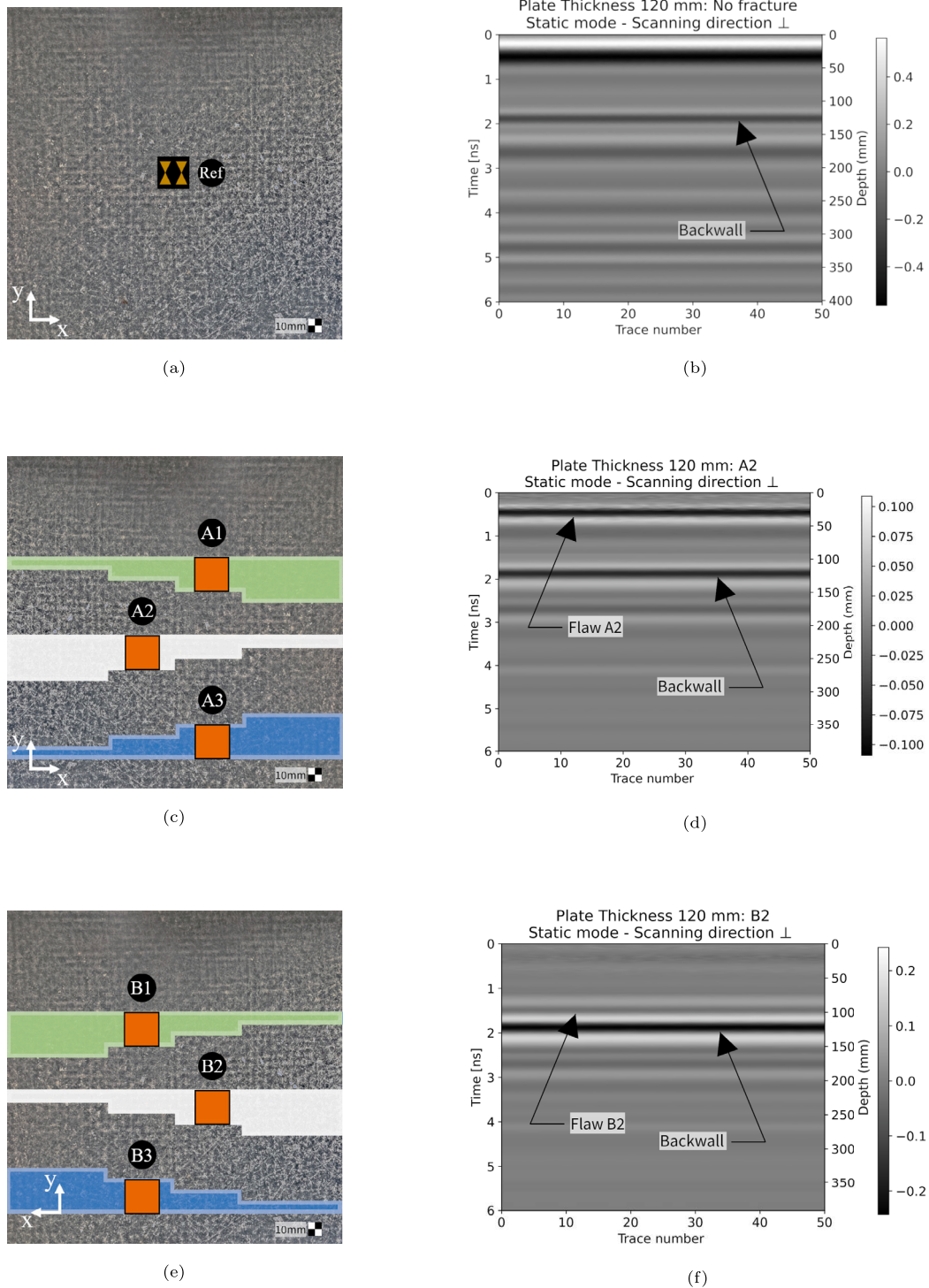
Fig. 10. An example of experimental data collection for the 120 mm specimen: (a) Location of reference scan. (b) Reference B-scan in a location having no damage. (c) Antenna static locations for the A-side. (d) B-Scan of the location 120A2⊥. (e) Antenna static locations for the B-side. (f) B-Scan of the location 120B2⊥.

expected to have significant effects on the accuracy of damage depth measurements. This is because the FRP specimen thicknesses in the present work were not large enough to cause significant loss of resolution for the present GPR system. For the deepest damages (120B3) in the 120 mm specimen, depth measurement was not possible because the responses from the specimen backwall masked the responses from the 120B3 damage. Despite the constraints of the present work (e.g., that the 2000 MHz "palm" antenna was the highest frequency antenna available), the results demonstrate a high success rate of the

technique in both locating damage and measuring their depth. It is speculated that with further optimization of the GPR survey for this application (e.g., higher antenna frequencies), the effectiveness of GPR used in this context would improve.

4.2.3. Water-filled damage (experimental)

For FRPs that are primarily used in marine environments (e.g., minehunter ships and tidal turbine blades), extensive structural damage and/or environmental aging could lead to water ingress into
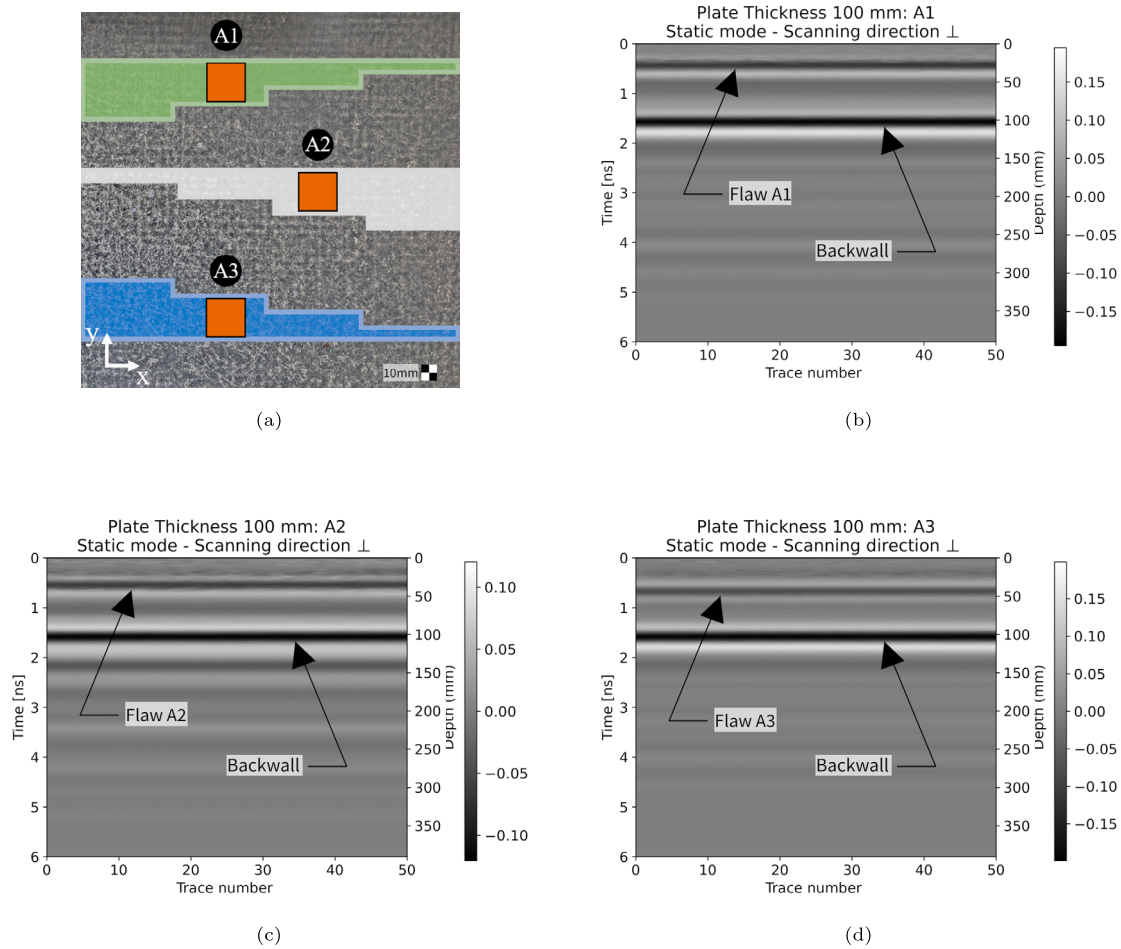
Fig. 11. Demonstration of the change in the experimentally observed depth of each damage: (a) Antenna static locations on the 100 mm specimen. (b) B-Scan of the location 100A1⊥. (c) B-Scan of the location 100A2⊥. (d) B-Scan of the location 100A3⊥.

Table 1
Detectability of damage from GPR experiment compared to the FMC-TFM ultrasound measurements from Refs. [10,32].

Damage Name	Specimen Thickness (mm)	Damage depth Actual (mm)	Damage depth Modeled (mm)	Damage depth GPR (mm)	FMC-TFM UT (mm)
100A1⊥	100	20	19.4	18.9	21.5
100A2⊥	100	30	28.6	27.2	28.0
100A3⊥	100	40	37.9	36.0	36.8
100A1//	100	20	20.8	17.8	21.5
100A2//	100	30	28.7	26.4	28.0
100A3//	100	40	38.1	35.8	36.8
100B1⊥	100	57	59.1	59.8	60.0
100B2⊥	100	67	66.5	67.8	69.2
100B3⊥	100	77	Not found	Not found	76.4
100B1//	100	57	56.7	57.1	60.0
100B2//	100	67	67.5	66.3	69.2
100B3//	100	77	Not found	Not found	76.4
120A1⊥	120	10	10.2	10.7	Not found
120A2⊥	120	20	20.2	19.7	Not found
120A3⊥	120	30	30.3	29.5	Not found
120A1//	120	10	9.9	10.5	Not found
120A2//	120	20	19.5	19.0	Not found
120A3//	120	30	28.6	27.1	Not found
120B1⊥	120	87	86.0	88.5	Not found
120B2⊥	120	97	97.7	98.6	Not found
120B3⊥	120	107	Not found	Not found	Not found
120B1//	120	87	87.6	87.4	Not found
120B2//	120	97	96.7	96.4	Not found
120B3//	120	107	Not found	Not found	Not found
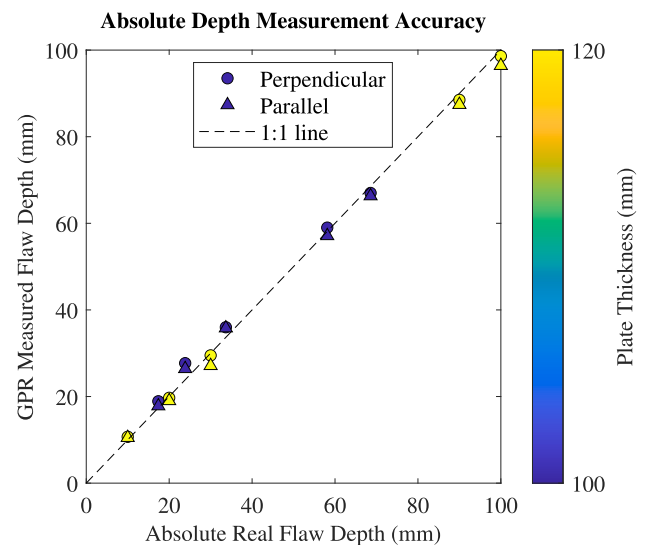
Fig. 12. Accuracy of GPR-measured damage depths.

the structure. Such water pockets or water saturation would likely degrade the mechanical performance of the FRP, and can accelerate/promote the propagation of damage within the structure [48–50]. For these reasons, it would be highly advantageous to detect water
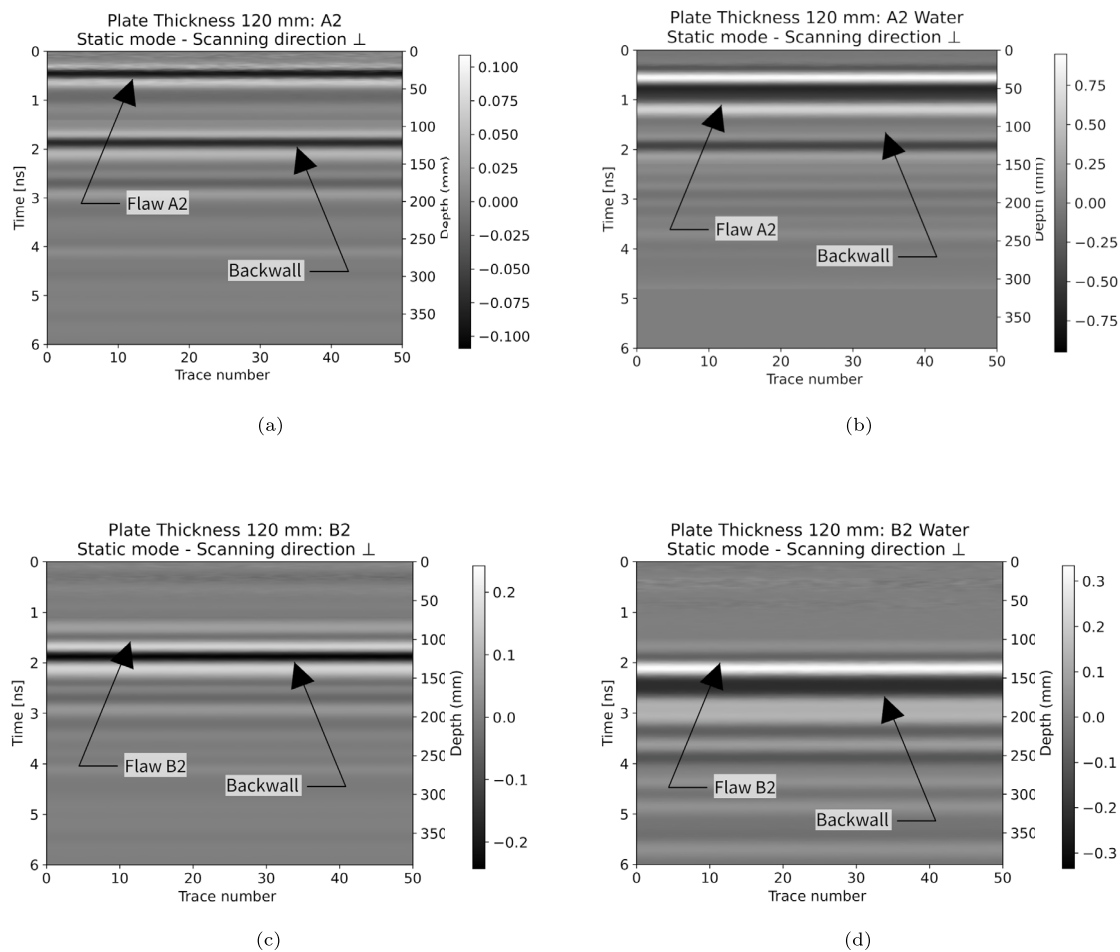
Fig. 13. An example showcasing how the presence of water inside a damage can affect the ability to detect it with GPR: (a) B-Scan from damage 120A2⊥ in the dry configuration. (b) Scan from damage 120A2⊥ with a water-filled damage. (c) B-Scan from damage 120B2⊥ in the dry configuration. (d) B-Scan from damage 120B2⊥ with a water-filled damage.

inside the structure when it is dry-docked for asset maintenance. To test the ability of GPR to detect water-filled damage features, the ability to detect dry damage was compared with their water-filled counterparts. This study was completed for all damage, however, for concision in the manuscript, only two water-filled delaminations are shown as a case study. Fig. 13 shows two representative cases in the 120 mm specimen, damage 120A2⊥, and damage 120B2⊥. The presence of water within a damage greatly increases the probability of its detection. This is an expected result, considering the higher relative permittivity of water (approximately 80 [27]) compared to the measured relative permittivity of the glass FRP used in this study (approximately 4.5) and air (1 [20]). The sharper gradient of permittivity transitioning from FRP to water (versus FRP to air) creates a larger returned signal amplitude. Furthermore, the location of the damage peak is shifted in time due to the slower propagation velocity of the EM wave through water, in comparison to air. This is a tell-tale, indicative sign to practitioners of GPR that water is present in a given structure. These findings were consistent for all damage in both specimens; the water filled delaminations produced detectable (and in most cases, high amplitude) responses when inspecting with GPR, even when the delamination through-thickness dimension was small relative to the FRP specimen thickness. Such observations are inherent to the GPR technique — given it exploits permittivity as previously discussed — and could be highly advantageous to the inspection of materials in the marine context, where extensive damage or aging in a structure could easily lead to the diffusion or even bulk flow of water into the structure [51,52], thereby potentially compromising its mechanical properties [48–50].

4.2.4. GPR antenna orientation (experimental)

The probability of detection of any target is theoretically maximized when the long axis of the bowtie antennas are in alignment with the long axis of any feature in the inspected part [34,53]. Consequently, the influence of antenna orientation during data capture — with respect to the geometric orientation of the target features — must be investigated. In the case of the present work, the greater probability of damage detection theoretically occurs when the survey direction is perpendicular to the damage (for example: A1⊥, A2⊥, A3⊥ etc.), and is theoretically lower in the scenario of parallel survey direction (damage A1//, A2//, A3// etc.). No difference was observed between the parallel and perpendicular static data acquisition orientations, neither before nor after processing. This is likely because the dry embedded damage in the FRP specimens were too thin, and the relative permittivity between the air-filled damage and the surrounding FRP material too similar, to cause sufficient contrasts. As such, both survey directions appeared to produce similar results. This is reinforced when considering the larger data set included in Table 1, where — regardless of antenna orientation during data acquisition — if damage was "not found" with one antenna orientation, the damage remained "not found" for both orientations. Comparatively, post-processing in the form of background removal had significantly greater impact on the ability to detect a given damage. To test this theory, damage 120A2 and 120B2 were sealed at both open ends and filled with water. The resulting scans are shown in Fig. 14, where small differences in the response between the antenna orientations with respect to the damage direction have been magnified by the larger difference between the relative permittivity of water and that of the FRP.
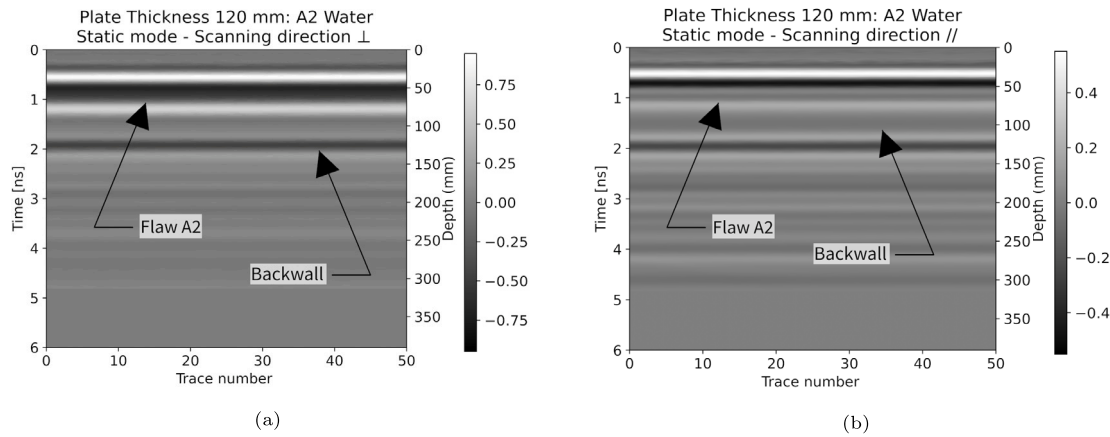
Fig. 14. An example showing how antenna orientation — with respect to the target — affects damage detection in water-filled damage: (a) Water-filled damage scanned perpendicular (damage 120A2⊥). (b) Water filled damage scanned parallel (damage 120A2//).

5. Comparison of GPR experimental data with ultrasound data

Comparison with a modern ultrasonic NDT method is provided to contextualize the GPR experimental results. For this comparison, data was gathered from recently published works [10,32] by the same research group, wherein the same FRP specimens were inspected using a full matrix capture (FMC) total focusing method (TFM) approach. The literature [10,32] utilized a Sonatest veo+ ultrasonic detector equipped with a Sonatest X6B-0.5M64E-2x10 (64 elements, 0.5 MHz) linear array probe. In the interest of concision in the present work, readers are directed towards the relevant literature [10,32] for any additional details concerning the ultrasonic inspection. Where the ultrasonic inspection was successful in locating the damage, data for the ultrasound-measured damage depth within the FRP specimen was captured for later comparison with the same measurements captured from the GPR experiments. In this way, it was possible to compare the likelihood of detecting a given damage feature with each technique, as well as to compare the accuracy of measuring the damage location with respect to the specimen thickness.

The available data from FMC-TFM ultrasound inspection of the same FRP specimens were gathered from literature and are presented in Table 1. The percentage difference in depth between the measured depth of damage (FMC-TFM or GPR) and the real, actual damage depth was calculated using Eq. (2). This created a metric to compare GPR with the FMC-TFM. Difference in depth measurement is plotted against damage depth in Fig. 15, where the dashed reference line represents an exactly accurate damage depth measurement (i.e. 0% difference).

$$\text{difference in depth measurement} = 100$$
$$\times \frac{\text{depth measured} - \text{actual damage depth}}{\text{actual damage depth}} \quad (2)$$

Although the measurement of damage depth (where available) is similar by both techniques, it is highlighted that the ultrasonic method used was unable to locate any damage in the 120 mm thick specimen. Discussions provided in the literature [32] state the inability of the particular ultrasound system to detect the specimen backwall in the 120 mm thick specimen. It is noted that this limitation may be specific to the particular ultrasound system used, however, it is indicative of the inspection limits of FMC-TFM ultrasound on thick FRPs in general. By contrast, in the GPR experiments most damage was detectable using GPR, and the specimen thickness had no identifiable effect on ability to inspect using this GPR system at these FRP thicknesses (≥100 mm). In the GPR experiments, two damage features were not found; these were the 100B3 and 120B3 damage features (regardless of the antenna alignment). This was previously explained by the close proximity of these features to the FRP specimen backwalls. When the damage is close to the specimen backwall, it is possible for the GPR response peaks from the damage to get masked or obscured inside the GPR response peaks from the backwall. Where this occurred, it was not possible to extract the response from the damage with any existing data processing techniques, and therefore, it was not possible to detect these damage features. Since the response captured from a damage feature is a function of the antenna frequency, the GPR setup, the FRP material system and the damage feature geometric and electrical properties, further study is required to identify the limits for how close damage can be located to the FRP backwall whilst still being detectable. Literature [10,32] highlights additional complexities associated with using FMC-TFM ultrasound to inspect thick FRP structures, for example, the presence of signal clutter that may act to obscure or hide a mechanically significant damage feature. Since FMC-TFM ultrasound exploits differences in propagation of sound waves through media, any feature that presents as a gradient in acoustic impedance can result in a similar response to the response from a damage feature. Examples of FRP features that can generate such signal clutter are interfaces between adjacent laminae, interfaces between fiber reinforcements and resins and resin-rich volumes. By contrast, all of the features listed do not present significant gradients in electrical properties, especially when compared to the gradient in electrical properties that is present at the boundary between an FRP and delamination damage (e.g., between FRP and air or water). Since GPR detects differences in electrical properties, it is less sensitive to these types of features. Therefore, there is comparatively less chance that this type of feature within the FRP would block the ability to find delamination damage, compared to FMC-TFM ultrasound.

In the referenced FMC-TFM ultrasound literature [10,32], the in-plane dimensions and profile of the damage were considered in the assessment of damage detectability. Therein, challenges associated with signal clutter and wave refraction were reported. In contrast to ultrasound, the step-like shape was not utilized in the present work, since GPR does not image and cannot size damage directly, especially when the thickness of features is less than the GPR's pulse length in the inspected material. Furthermore, inverse scattering for GPR imaging is not available beyond theoretical academic research. Imaging the geometry of the damage is presently a very complex and computationally demanding problem of active research.

As can be seen in this comparison, there are several key advantages to using GPR for inspection of thick FRP structures. These can be summarized as: 1. GPR detects differences in electrical properties, so is less sensitive to benign differences between FRP constituents, 2. GPR has been used to inspect comparatively much thicker structures, and as such, should be better positioned to inspect thicker FRPs than would be possible with existing techniques e.g., ultrasound. Nevertheless, it is not proposed that GPR should replace ultrasound for
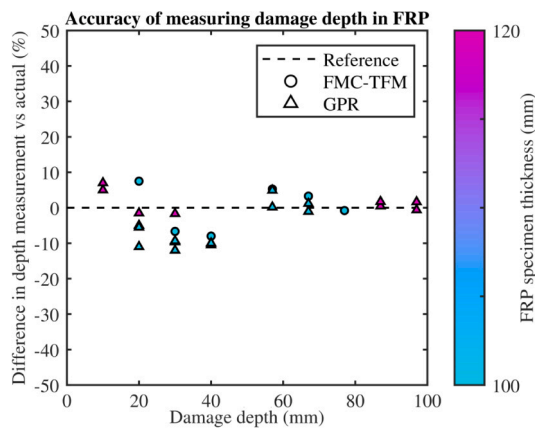
Fig. 15. Accuracy of GPR-measured damage depths compared to accuracy of ultrasound-measured damage depths.

the inspection of all thick FRPs; it is proposed that GPR could be used alongside other techniques towards the complete inspection of thick FRPs. With regard to inspecting structures that are not glass-FRP laminates (e.g., carbon-FRPs, sandwich structures, hybrid structures), if the structure to be inspected has low electrical conductivity, then it may be a good candidate for GPR inspection. However, GPR cannot be applied to carbon-FRPs, since they have very high electrical conductivity and signal penetration is therefore not possible. This opens up an exciting avenue for future research: evaluating and demonstrating the applicability of GPR to other material systems, structure types and different damage configurations.

6. Conclusions

The efficacy of GPR to detect delamination damage features in thick section FRP composites was evaluated, using a 2000 MHz GPR system. Delaminations were generated during manufacturing of ultra-thick ($\geq$100 mm) FRP specimens, which ranged in total specimen thickness from 100 to 120 mm. Specimen thickness, damage depth location, antenna orientation and damage dryness were selected as test variables. Modeling of the inspection using gprMax showed promising feasibility, and after the real data had been analyzed, high correlation was observed between the real and synthetic data. This research proves that dry, 3 mm thick, in-plane damage can be discovered and located with this GPR setup, using unmodified equipment and common background removal processes. Measuring the depth location of each damage feature proved to be highly accurate, with good agreement between measured data and actual location. Most damage features were clearly observed in both the A- and B-scans, with difficulty in inspection only when a damage feature was positioned very close to the specimen back wall, where the stronger back wall signal sometimes obscured the damage response. When damage features were filled with tap water, inspection became comparatively simple, as the response from water showed clearly in the data (attributed to the high relative permittivity of water compared to the composite and to air), with the characteristic response delays and strong reflections that water typically exhibits in ground radar inspection. Such a result has clear advantage for FRP structures that are deployed in the marine context, where extensive damage could lead to water-saturation or localized water-pockets in a structure. In a comparison with a FMC-TFM ultrasound inspection method, the GPR system proved superior at detecting damage features in thicker FRP structures (>100 mm), whilst retaining comparable depth measurement accuracy to the ultrasonic method across the test matrix. It is proposed that GPR could be used alongside other techniques towards the complete inspection of thick FRPs. Since the efficacy of GPR in this application was previously unknown, the

findings presented herein constitute a significant contribution to the field of NDT of FRPs. As such GPR has the potential to enable more efficient maintenance procedures, and empower operators to improve structural safety, in all sectors which use thick FRP structures.

CRediT authorship contribution statement

James A. Quinn: Writing – review & editing, Writing – original draft, Validation, Resources, Methodology, Investigation, Formal analysis, Conceptualization. **Ourania Patsia:** Writing – review & editing, Writing – original draft, Software, Resources, Methodology. **Antonios Giannopoulos:** Writing – review & editing, Writing – original draft, Software, Resources, Methodology. **Conchúr M. Ó Brádaigh:** Writing – review & editing, Writing – original draft, Supervision, Funding acquisition, Conceptualization. **Edward D. McCarthy:** Writing – review & editing, Writing – original draft, Supervision, Project administration, Funding acquisition.

Declaration of competing interest

The authors declare that they have no known competing financial interests or personal relationships that could have appeared to influence the work reported in this paper.

Data availability

Data will be made available on request.

Acknowledgments

References

[1] Taheri H, Hassen AA. Nondestructive ultrasonic inspection of composite materials: A comparative advantage of phased array ultrasonic. Appl Sci 2019;9(8):1628. http://dx.doi.org/10.3390/app9081628.

[2] Wang B, Zhong S, Lee TL, Fancey KS, Mi J. Non-destructive testing and evaluation of composite materials/structures: A state-of-the-art review. Adv Mech Eng 2014;12(4):1–28. http://dx.doi.org/10.1177/1687814020913761.

[3] Li D, Zhou J, Ou J. Damage, nondestructive evaluation and rehabilitation of FRP composite-RC structure: A review. Constr Build Mater 2021;271(121551). http://dx.doi.org/10.1016/j.conbuildmat.2020.121551.

[4] Thomas JA. HMS wilton - a glass-reinforced plastics minehunter. Composites 1972;3(2):79–82. http://dx.doi.org/10.1016/0010-4361(72)90380-1.

[5] Hall DJ, Robson BL. A review of the design and materials evaluation programme for the GRP/foam sandwich composite hull of the RAN minehunter. Composites 1984;15(4):266–76. http://dx.doi.org/10.1016/0010-4361(84)90707-9.

[6] Tran P, Wu C, Saleh M, Bortolan Neto L, Nguyen-Xuan H, Ferreira AJ. Composite structures subjected to underwater explosive loadings: A comprehensive review. Compos Struct 2021;263(113684). http://dx.doi.org/10.1016/j.compstruct.2021.113684.

[7] Hsu DK, Minachi A. Defect characterization in thick composites by ultrasound. In: Thompson DO, Chimenti DE, editors. Review of progress in quantitative nondestructive evaluation. Boston, MA: Springer US; 1990, p. 1481–8. http://dx.doi.org/10.1007/978-1-4684-5772-8_190.

[8] Mouritz AP. Ultrasonic and interlaminar properties of highly porous composites. J Compos Mater 2000;34(3):218–39. http://dx.doi.org/10.1177/002199830003400303.

[9] Kersemans M, Verboven E, Segers J, Hedayatrasa S, Paepegem WV. Non-destructive testing of composites by ultrasound, local defect resonance and thermography. Proceedings 2018;2(8). http://dx.doi.org/10.3390/ICEM18-05464.

[10] Quinn JA, Davidson JR, Bajpai A, Ó Brádaigh CM, McCarthy ED. Advanced ultrasonic inspection of thick-section composite structures for in-field asset maintenance. Polymers 2023;15(15). http://dx.doi.org/10.3390/polym15153175.

[11] Ibrahim ME. Nondestructive testing and structural health monitoring of marine composite structures. In: Marine applications of advanced fibre-reinforced composites. Elsevier Inc.; 2016, p. 147–83. http://dx.doi.org/10.1016/B978-1-78242-250-1.00007-7.

[12] Jeong H, Lee J-R. Investitation of mobile ultrasonic propagation imager as a tool for composite wind blade quality control. Compos Struct 2015;133:39–45. http://dx.doi.org/10.1016/j.compstruct.2015.07.091.

[13] Mouritz A, Townsend C, Shah Khan M. Non-destructive detection of fatigue damage in thick composites by pulse-echo ultrasonics. Compos Sci Technol 2000;60(1):23–32. http://dx.doi.org/10.1016/S0266-3538(99)00094-9.

[14] Daniels DJ. Ground penetrating radar. second ed.. Institution of Engineering and Technology (The IET); 2004.

[15] Wai-Lok Lai W, Dérobert X, Annan P. A review of ground penetrating radar application in civil engineering: A 30-year journey from locating and testing to imaging and diagnosis. NDT&E Int 2018;96:58–78. http://dx.doi.org/10.1016/j.ndteint.2017.04.002.

[16] Alani AM, Aboutalebi M, Kilic G. Applications of ground penetrating radar (GPR) in bridge deck monitoring and assessment. J Appl Geophys 2013;97:45–54. http://dx.doi.org/10.1016/j.jappgeo.2013.04.009.

[17] Benedetto A, Tosti F, Ciampoli LB, D'Amico F. GPR applications across engineering and geosciences disciplines in Italy: A review. IEEE J Sel Top Appl Earth Obs Remote Sens 2016;9(7):2952–65. http://dx.doi.org/10.1109/JSTARS.2016.2554106.

[18] Giannakis I, Giannopoulos A, Warren C. A realistic FDTD numerical modeling framework of ground penetrating radar for landmine detection. IEEE J Sel Top Appl Earth Obs Remote Sens 2015;9(1). http://dx.doi.org/10.1109/JSTARS.2015.2468597.

[19] Pettinelli E, Cosciotti B, Lauro SE, Mattei E. An overview of GPR subsurface exploration of planets and moons. Lead Edge 2022;41(10):672–80.

[20] Annan AP. Electromagnetic principles of ground penetrating radar. In: Jol HM, editor. Ground penetrating radar theory and applications. Amsterdam: Elsevier; 2009, p. 1–40. http://dx.doi.org/10.1016/B978-0-444-53348-7.00001-6.

[21] Halabe U, Dutta S, Hota G. Infrared thermographic and radar testing of polymer-wrapped composites. Mater Eval 2010;68:447–51.

[22] Pyakurel S, Halabe U. 2D and 3D imaging of concrete and fiber reinforced polymer composite wrapped cylindrical columns using ground penetrating radar. Mater Eval 2013;71:73–82.

[23] Zatar WA, Nguyen HD, Ngheim HM, Cogsun C. Non-destructive testing of GFRP-wrapped reinforced-concrete slabs. In: Transport research board annual meeting: 1298 - nondestructive testing and evaluation of bridges. Washington DC, United States: Transportation Research Board; 2021.

[24] Jaishankar P, Kanchidurai S, Cyril Thomas A, Saravana Raja Mohan K. Experimental investigation on non-destructive behaviour of repaired FRP concrete beams. Mater Today: Proc 2022;64:990–4. http://dx.doi.org/10.1016/j.matpr.2022.05.078.

[25] Hing CLC, Halabe UB. Nondestructive testing of GFRP bridge decks using ground penetrating radar and infrared thermography. J Bridge Eng 2010;15(4):391–8. http://dx.doi.org/10.1061/(asce)be.1943-5592.0000066.

[26] Halabe UB, Hing CL, Klinkhachorn P, Gangarao HV. Subsurface defect detection in FRP bridge decks using ground penetrating radar. In: AIP conference proceedings. Vol. 894, 2007, p. 1443–52. http://dx.doi.org/10.1063/1.2718136.

[27] Davis J, Annan P. Ground-penetrating radar for high-resolution mapping of soil and rock stratigraphy. Geophys Prospect 1989;37(5):531–51. http://dx.doi.org/10.1111/j.1365-2478.1989.tb02221.x.

[28] Drozdov AD, deClaville Christiansen J. Modelling dielectric permittivity of polymer composites at microwave frequencies. Mater Res Bull 2020;126(110818). http://dx.doi.org/10.1016/j.materresbull.2020.110818.

[29] Ibrahim ME. Nondestructive evaluation of thick-section composites and sandwich structures: A review. Composites A 2014;64:36–48. http://dx.doi.org/10.1016/j.compositesa.2014.04.010.

[30] Nsengiyumva W, Zhong S, Lin J, Zhang Q, Zhong J, Huang Y. Advances, limitations and prospects of nondestructive testing and evaluation of thick composites and sandwich structures: A state-of-the-art review. Compos Struct 2021;256(112951). http://dx.doi.org/10.1016/j.compstruct.2020.112951.

[31] Geophysical Survey Systems Inc. Antennas manual. Tech. rep., MN30-903 R, Geophysical Survey Systems Inc; 2017, p. 7–14.

[32] Quinn J. Asset maintenance of thick section fibre-reinforced composite structures (Ph.D. thesis), The University of Edinburgh; 2024, http://dx.doi.org/10.7488/era/4513.

[33] Hatsukade Y, Inaba T, Kasai N, Maruno Y, Ishiyama A, Tanaka S. Detection of deep-lying defects in carbon fiber composites using SQUID-NDE system cooled by a cryocooler. Phys C: Supercond 2004;412–414:1484–90. http://dx.doi.org/10.1016/j.physc.2004.01.145, Proceedings of the 16th International Symposium on Superconductivity (ISS 2003). Advances in Superconductivity XVI. Part II.

[34] Porsani JL, Slob E, Lima RS, Leite DN. Comparing detection and location performance of perpendicular and parallel broadside GPR antenna orientations. J Appl Geophys 2010;70(1):1–8. http://dx.doi.org/10.1016/j.jappgeo.2009.12.002.

[35] Annan P. Ground penetrating radar principles, procedures and applications. Sensors & Software; 2003.

[36] Jung-Ho Kim, Seong-Jun Cho, Myeong-Jong Yi. Removal of ringing noise in GPR data by signal processing. In: Geosciences journal. Vol. 11, 2007, p. 75–81.

[37] Nobes DC. Geophysical surveys of burial sites: A case study of the oaro urupa. Geophysics 1999;64(2):357–67. http://dx.doi.org/10.1190/1.1444540.

[38] Warren C, Giannopoulos A, Giannakis I. Gprmax: Open source software to simulate electromagnetic wave propagation for ground penetrating radar. Comput Phys Comm 2016;209:163–70.

[39] Patsia O, Giannopoulos A, Giannakis I. Developing a realistic numerical equivalent of a GPR antenna transducer using global optimizers. Near Surf Geophys http://dx.doi.org/10.1002/nsg.12280.

[40] Patsia O, Giannopoulos A, Giannakis I. A digital twin of the GSSI 2000 MHz palm antenna developed using multi-parametric optimisation. In: Proceedings of the 11th international workshop on advanced ground penetrating radar (IWAGPR), Valletta, Malta. 1–4 December 2021.

[41] Patsia O. Deep learning processing and interpretation of ground penetrating radar data using a numerical equivalent of a real GPR transducer (Ph.D. thesis), The University of Edinburgh; 2023, http://dx.doi.org/10.7488/era/3233.

[42] Tahir DA, Jamal GM, Abdullah OG. Influence of woven roving fiber E-glass on electrical properties of polyester composite. Al-Nahrain J Sci 2013;16(3):124–8.

[43] Manju M, Vignesh S, Nikhil K, Sharaj A, Murthy M. Electrical conductivity studies of glass fiber reinforced polymer composites. Mater Today: Proc 2018;5(1, Part 3):3229–36. http://dx.doi.org/10.1016/j.matpr.2018.02.027, International Conference on Advanced Materials and Applications (ICAMA 2016), June 15-17, 2016, Bengaluru, Karanataka, INDIA.

[44] Słupkowski T. Electrical conductivity of polyester polymer containing carbon black. In: Görlich, editor. Physica status solidi / A.. Vol. 90, Berlin, Boston: De Gruyter; 1985, p. 737–42. http://dx.doi.org/10.1515/9783112494806-038.

[45] Gao X, Cheng L, Tan J, Yang W. Conductive nanocarbon-coated glass fibers. J Phys Chem C 2020;124:17806–10. http://dx.doi.org/10.1021/acs.jpcc.0c03948.

[46] Kupke M, Wentzel H-P, Schulte K. Electrically conductive glass fibre reinforced epoxy resin. Mater Res Innov 1998;2:164–9. http://dx.doi.org/10.1007/s100190050079.

[47] Balanis CA. Advanced engineering electromagnetics. Wiley; 2012.

[48] Alam P, Robert C, Ó Brádaigh CM. Tidal turbine blade composites - a review on the effects of hygrothermal aging on the properties of CFRP. Composites B 2018;149:248–59. http://dx.doi.org/10.1016/j.compositesb.2018.05.003.

[49] Huang G, Hongxia S. Effect of water absorption on the mechanical properties of glass/polyester composites. Mater Des 2007;28(5):1647–50. http://dx.doi.org/10.1016/j.matdes.2006.03.014.

[50] Mamalis D, Floreani C, Ó Brádaigh CM. Influence of hygrothermal ageing on the mechanical properties of unidirectional carbon fibre reinforced powder epoxy composites. Composites B 2021;225(109281). http://dx.doi.org/10.1016/j.compositesb.2021.109281.

[51] Davies P. Environmental degradation of composites for marine structures: new materials and new applications. Phil Trans R Soc A 2016;374(20150272). http://dx.doi.org/10.1098/rsta.2015.0272.

[52] Davies P. Toward more representative accelerated aging of marine composites. In: Lee SW, editor. Advances in thick section composite and sandwich structures. Springer Nature Switzerland AG; 2020, http://dx.doi.org/10.1007/978-3-030-31065-3.

[53] Utsi EC. Ground penetrating radar: theory and practice. Butterworth-Heinemann; 2017.